University of Crete

Department of Materials Science and Technology

Batchelor's Thesis

"*Quantification of mussel byssal plaque porosity*"

Ioannis Sampson

June 2022

Table of Contents

Acknowledgements

Special thanks go to Prof. E. Filippidi for her guidance and for giving me the opportunity to work on the project. I would like to thank S. Papadogiorgaki and S. Papadakis at the Biology department of the University of Crete for their help with electron microscopy and sample preparation. I would like to thank Drs. K. Keklikoglou and E. Chatzinikolaou from the institute of Marine Biotechnology and Aquaculture of the Hellenic Centre for Marine Reaserch (HCMR) for the micro CT measurements they performed on my samples and for their insightful discussions. I would like to thank T. Steriotis from the institute of Nanoscience and Nanotechnology of the National Center for Scientific Research (NCSR) "Demokritos" for his discussions on mercury porosimetry. I would like to thank S. Stamatiadis for giving me access to hardware and setting up ilastik, K. Papadopoulos for helping me find a microscopy ruler, O. Tsilipakos with my script in Matlab, Profs. Cruz Orive Luis M. and Cruz Rodriquez Marcos from the university of Cantabria for the stereology suggestions and discussions. Finally, I would like to thank my committee members Prof. A. Mitraki and Dr. T. Dailianis for their trust and encouragement. Lastly, a big thanks to my family and friends for the support.

List of Tables

List of Figures

I. Introduction

Mussels, in their natural habitat, attach to rocks, piers, or other mussels utilizing their byssus (Fig. 1a). The byssus is composed of a distal, adhesive, spatula-shaped plaque connected to a collagen-rich thread with a stiff distal portion and a pliable proximal portion (1). Proximally, the thread terminates at a muscle-controlled tissue inside the mussel shell. The mechanical interface between the thread and the plaque takes place inside the plaque, where collagen strands from the thread's core penetrate the plaque. The plaque's adhesive properties derive from Dopa (3,4-dihydroxyphenyl-L-alanine), a catecholic amino acid in mussel foot proteins (Mfps)(1, 2). Even though not all Mfps have been fully characterized yet, the architecture of the plaque is well defined (3). Over 20 different proteins compose the byssal plaque (4)The most abundant proteins are the Mfp-2, -3, -5, and -6 localized in the interior and at the interface with the substrate (e.g. Mfp-3 and -5). The plaque is protected at its top surface with a proteinaceous cuticle, mainly composed of Mfp-1 (1) (Fig.1).

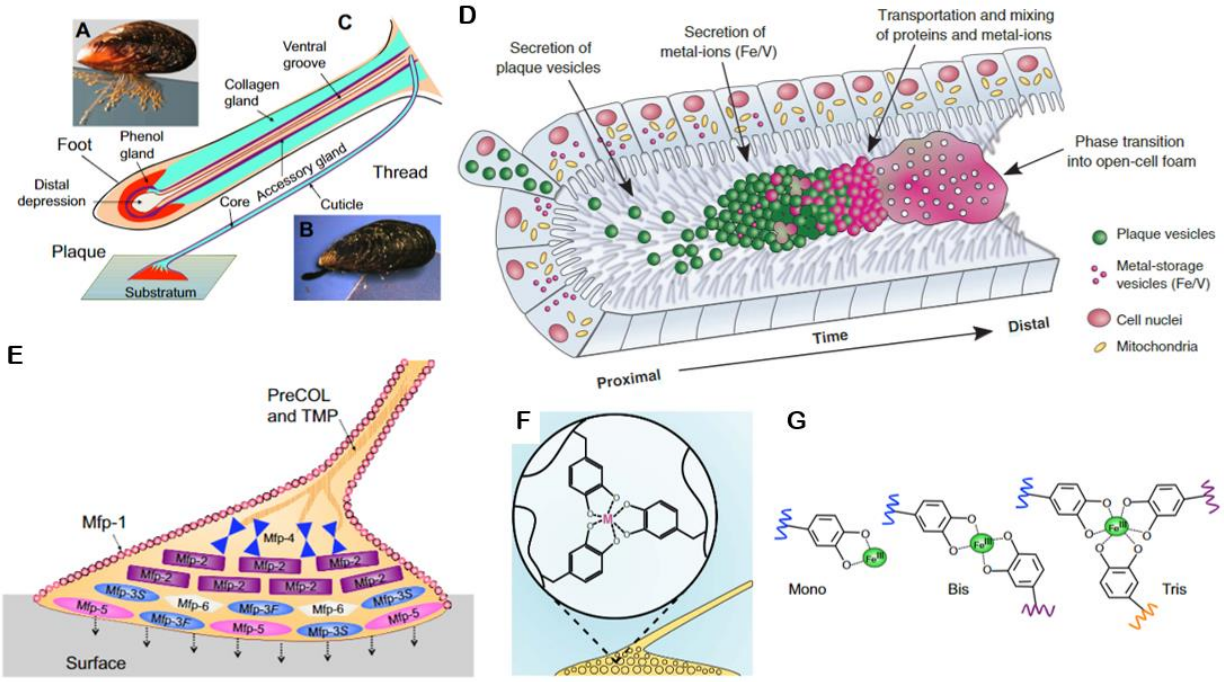

Fig. 1 Mussel byssal plaque anatomy and formation: (A) The mussel byssus attached to a substratum (1). (B) The mussel's foot emerging from the shell (1). (C) Anatomy of the foot (1). (D) A schematic model of the molecular component secretion during plaque formation (5). (E) Chemical profile of the plaque (1). (F) Schematic representation of the DOPA-Metal (M) coordinated cross-links, crucial for the porous plaque adhesion(5). (G) metal iron (Fe) mono bis and tris coordinated Dopa molecules (1).

The formation of the byssus is performed in a two-step process by the mussel's foot (1). The first is a transitory stage where molecular components are assembled at the collagen gland (ventral groove) and at the phenol gland (distal depression) of the foot. During plaque formation, plaque vesicles and metal storage particles (MSPs) mix, and iron and vanadium metal ions diffuse out of the MSPs throughout the dense protein phase forming pH-dependent DOPA-metal coordination bonds (6) (Fig.1d). These components are then secreted onto the candidate surface at an acidic environment ($pH \cong 2$) (4). The foot withdraws, exposing the secreted components (polyelectrolytic proteins) to the sea water, ($pH \cong 8$) aiding in the solidification of the byssal plaque-thread system under tension (1). The pH-dependance of the Dopa-metal (mono, bis, tris) coordination bonds has been reported to affect pore formation with pH perturbation (7). The tension applied provides stability, helping mussels anchor themselves to the substrate in order to withstand the forces from sea waves.

Mussels of the genus *Mytilus* have previously been reported to exhibit a foam-like interior (3) composed of large pores embedded in a fine pore mesh. However, mussels of the genus *Geukensia demissa*, found buried in tidal sea marshes of Florida, exhibit no such plaque interior architecture. Furthermore, mussels of the species *Perna canaliculus* exhibit significantly distinct large to mesh pore ratios (6) (Fig.2). If there is a mechanical advantage for adhesion, we expect there to be a correlation between habitat and pore formation; for instance, mussels in wave-swept habitats may have evolved to have pores, whereas those buried in the sand evolved not to have.

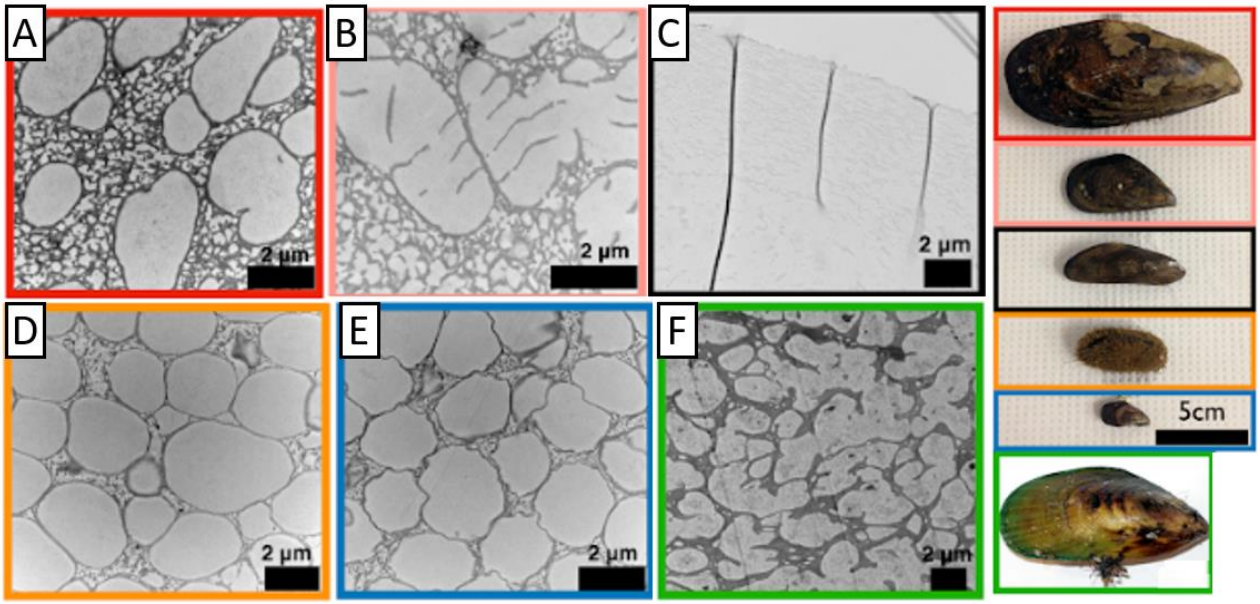

Fig. 2 TEM scans of different mussel species exhibiting porous plaque interior: (A) *Mytilus californianus*. (B) *Mytilus galloprovincialis*. (C) *Geukensia demissa*. (D) *Modiolus capax*. (E) *Septifer bifurcatus*. (F) *Perna canaliculus*.

An interesting aspect of the porous plaque is that it operates under tension, as opposed to the use of dry foam structures in engineering design which operate under compression e.g. helmets, seat cushions. Thus, we hypothesize that the mechanical advantage may be bestowed via the mechanics of fluid-filled pores, and may be described by the mechanics of poroelasticity. For a fluid infiltrated porous material, its mechanical strength resisting compression resides on the size, shape, orientation and distribution of the

pores (7). Upon stress, it is stated that the shear rate of deformation is counteracted by the viscosity of the fluid meaning that the system is not static (8). Our long-term goal is to learn enough about the material to be able to model it and possible 3d print it for simulated and actual mechanical tests. Another interesting unanswered question related to extra-organismal protein assembly is how is this final foam structure formed starting from a liquid solution protein secretion and what makes it different or modulates it among different mussel species.

To examine the plaque architecture, plaque samples had to be collected from mussels. *Mytilus galloprovincialis* mussels were selected due to regional accessibility (Crete) and seasonal availability. In order to quantitatively describe such structure in terms of mechanics –down the road, compare with other genera and understand how proteins lead to that structure upon pH change– we aim to quantitively measure the pores. To obtain high resolution images of the plaque architecture, electron microscopy and nano computer tomography (CT) may be used. Ideally, focused ion beam scanning electron microscopy (FIB-SEM) would give a better insight of the plaque's pore shape and volume distribution. To support an application for the need for FIB-SEM and nanoCT access and to ensure we are capable of sample collection in Crete, in this thesis focus was shifted towards more traditional electron microscopy techniques such as TEM, SEM, optical microscopy, and exploration of mercury porosimetry and micro tomography, such as microCT. Each technique posed different advantages and disadvantages. Below I discuss their (dis)advantages with respect to this project.

Scanning electron microscopy (SEM)

Scanning electron microscopy provides a great overview of the pores exposed at the surfaces of the plaque sections. However, exactly because of the depth perspective, pore walls, struts, and open pores are visible, creating a complex pixel intensity profile that while very perceptible –for the human eye– it is extremely hard to analyze by image analysis.

Transmission electron microscopy (TEM)

Transmission electron microscopy of thin ($\sim 100nm$) plaque sections provides high definition 2D images that cut through the pores and allow the clear definition of walls and struts and the doubly porous interior. The downside of this method is that due to the high magnification, TEM images represent only a fraction of the full plaque section. Thus, a quantitative assumption would be biased and incorrect unless we image wide, representative sections.

Optical microscopy

Optical microscopy images provide adequate information when a thin section of the sample (1μm) is observed. Although lacking in resolution, the size and distribution of the large pores are clearly visible. A systematic random selection of sample sections (2D) can be used to estimate the volume (3D) of the pores using the Cavalieri Method (9).

Mercury porosimetry

Mercury porosimetry is an extremely useful characterization technique capable of investigating total void volumes in a material having pores between 500 μm and 3.5 nm diameter through mercury infiltration under high pressure. The limitation factor of the technique resides on the fact that it is unable to detect closed pores since the mercury has no entry point. Also, the extremely high pressures applied in order to infuse the mercury inside the pores can rapture pore walls and even collapse the whole sample structure (10).

Micro-CT

Micro computer tomography is a 3D imaging technique that captures a series of 2D planar X-ray images which are later reconstructed into cross-section slices. These slices reveal the internal features and

when processed into a 3D model provide volumetric information of the microstructure (11). The volumetric resolution (voxel) is 1 μm.

Nano-CT

Similar to the micro-CT, X-ray 2D planar scans of an object can be obtained and further processed in to a 3D analogue. Nano computer tomography system allows for clear visualization of structures on the level of internal ultrastructure with a resolution of the flat-panel detector at the 50 nm scale (11). However, it only permits visualization of a small ROI, of maximum 24 μm x 24 μm sample width and depth, but large (~1 mm) height.

Image analysis & segmentation

Image segmentation was the main focus of the analysis. The principle of segmenting a digital image into groups with each group having a distinct characteristic provides information of the sample's component makeup. There are many algorithms used for segmentation and cell counting such us Cellpose (12), CountEM (13), trainable Waikato Environment for Knowledge Analysis (WEKA) segmentation plugin in FIJI (14), ilastik (15) etc. However, the images at hand exhibited various configurations of complex geometrical shapes (multidisperse system)(16) which could be best analyzed by neural network algorithms. Therefore, the selected algorithms were WEKA and ilastik. Ilastik is an free interactive learning and segmentation tool capable of segmenting, classifing, tracing and counting cells on experimental data. Its versatility and ease of use makes it a perfect candidate for processing histology images. On the other hand, trainable WEKA segmanetation is a FIJI plugin that produces pixel-based segmentations. WEKA can itself be called from the plugin which contains a collection of machine learning algorithms for data mining tasks. In particular, tools for data preparation, classification, regression, clustering, association rules mining, and visualization are written in the Java programming language. Comparing the two algorithms segmentation using ilastik (Fig. 2C) provides a better description of the individual features with sharper edges and less error (Fig. 3).

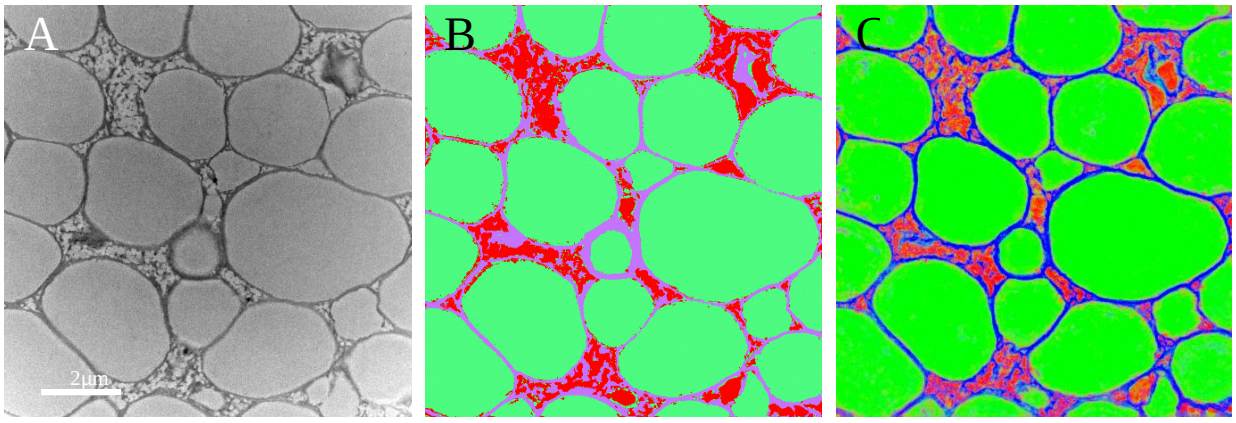

Fig. 3 Segmented images (A) TEM raw data image from *Modiolus capax* byssal plaque by Daniel DeMartini (UCSB, 2018). Scalebar 2 μm. Example of segmented image using trainable WEKA segmentation plugin in FIJI (B) versus ilastik (C).

II. Materials and Methods

Mussels

Fresh mussels, purchased from the supermarket, were cleaned individually removing excess byssal plaques present on their shells and got transferred to the nearest sea. Emerging them in to the sea for about half an hour ensured mussels rehabilitation. Alive rehabilitated mussels were placed in an 10L aquarium tank filled with sea water (~19℃) and were transferred in the lab. To ensure water flow and oxygenation the aquarium was fitted with 2 bubble stones attached to an electric pump. In addition, an acrylic sheet $20 \times 25\ cm$ was placed at the bottom of the tank on which mussels were to deposit their adhesive byssal plaques. Mussel's longevity was ensured by frequent water changes (every 1-2 days) and immediate discard of any dead ones.

Byssal plaque isolation

Active mussels produced byssal plaques almost daily, hence the extraction procedure occurred as follows: the acrylic sheet was removed from the aquarium on to the work bench. Mussels that had not attached themselves on to the acrylic sheet were placed back in to the water. Due to the fact that the byssal plaque-thread system is under tension because of a muscle inside the mussel controlling the mussel to substrate attachment, a slight pull on the thread towards the plaque should be applied, by hand, close to the mussel. Then, a clean cut could be performed close to the mussel's shell using a razor blade. By repeating the process for all plaques, we were left with the plaques attached to the substrate, which were then rinsed with clean water. Isolating the plaque-thread system from the substrate was achieved by a clean sweeping cut with the razor blade separating plaque from the plastic substrate. Using tweezers, plaques were placed in DI water-filled Eppendorf tubes (1.5 ml), labeled and stored in the fridge (4℃).

Byssal plaque preservation protocol

Collected plaques were placed individually in a 50 ml Eppendorf tube in DI water. Two washes with DI water were performed before gradually changing the solvent to a 70% ethanol solution. Steady increments of 30%, 50%, 70% ethanol in water solutions with a 10 min rest in between steps were carried out.

SEM preparation

Mussel byssal plaque samples harvested at two different days were selected for SEM preparation. They were stored in deionized water at 4°C. For critical point drying (BAL-TEC CPD 030 critical point dryer), plaques were placed in plastic porous cups within a jar on ice. A solution of 2% formaldehyde and 2.5% glutaraldehyde fixation buffer (what is inside?) was added and left for 30 min. Samples were sequentially washed in 30%, 50%, 70%, 90%, 100%, 100% ethanol solutions with a 10 min rest in between washes. The last exchange was with a 100% chromatography grade dry ethanol. Finally, samples were placed in the critical point drying chamber.

Dry samples were placed on a glass substrate with an adhesive tape at different orientations. Samples were then Sputter coated with Au for 59s, yielding a 5nm film Au coating using the BAL-TEC SCD 050 sputter coater. SEM was performed at 20 kV with JEOL JSM-6390LV scattering electron microscope.

TEM preparation

Plaques harvested 48h prior were fixated in 1.5 ml buffer #1 for 50 h. Buffer #1 consisted of 2% Formaldehyde, 2.5% Glutaraldehyde, 0.2 M sodium cacodylate, 0.3 M sodium chloride in nanopure water. Samples underwent 3 consecutive washes with a 10 min resting window in degassed buffer #2 (0.2 M sodium cacodylate in nanopure water and 0.3 M sodium chloride, pH 7.2). All buffers were degassed using ElmaSonic S ultrasonic cleaning Unit for 5 mins. Samples were post fixed in 2% osmium Tetroxide in buffer #3 (0.4 M sodium cacodylate and 0.6 M sodium chloride in nanopure water) for 2 h.

The mixture was then replaced by buffer #2 and left overnight in the fridge (4°C). Repeated (about 5 times) nanopure water washes were performed in order to remove excess osmium tetroxide. Samples were sequentially washed in 25%, 50%, 75%, 90%, 100%, 100% ethanol solutions with a 10-15 min rest in between. Solvent was slowly switched to propylene oxide by introducing propylene oxide mixtures of 33%, 66%, 100%, 100%, 100% in ethanol for 10-15 min each. A 33%, 66%, 100% epoxy resin in ethanol solution was used for the infiltration step. Epoxy resin (DURKOPAN ™) consisted of a four-component mixture of A: single component A (epoxy resin), B: single component B (hardener 946), C: single component C (accelerator), D: single component D (plasticizer). The infiltration step took place under constant mixing on a mechanical stirrer. Samples remained in 33% solution (epoxy resin in propylene oxide) for 2h, in 66% solution for 16h followed by another 66% solution wash for 24 h. Lastly, two washes in 100% resin were performed for 24h each before the samples where carefully placed in silicon molds and in the oven at 60°C for 48 h for them to dry.

Following standard TEM procedures chosen sample got trimmed and were cut by an LKB BROMMA 2088 ULTRATOME microtome. Thin sections of about 100 nm were mounted on the matt surface of 300 Mesh 3.05 mm copper TEM grid and post stained on drops of Uranyl acetate 98% followed by Tri-Sodium citrate (Mallinckrodt®). Samples were investigated with a JEOL JEM-2100 electron microscope operating at 80kV Images were captured by Gatan Erlangshen ES500W camera with a magnification setting of $\times\ 3K$ at 1 μm images and $\times\ 2K$ at 2 μm images with a size of $4008 \times 2884\ pixels$.

Optical microscopy preparation

Plaques encapsulated in resin (TEM samples) were thinly sliced using LKB BROMMA 2088 ULTRATOME microtome. Sections about 1 μm thick were placed on a microscope glass slide ($3 \times 1\ inch$) and stained with Methylene blue. Excess methylene blue was dried off using a hot plate (LKB 2208 MULTIPLATE). Sections were fit with Biomount mounting medium and a microscopy glass cover slip No.1 $18 \times 18\ mm$. Samples were investigated with a NIKON ECLIPSE E800 microscope. Images were captured using the software $ProgRes$® CapturePro28.8-JENOPTIK optical system. Image size was $1360 \times 1024\ pixel$. Magnification 60x was obtained with an oil immersion lens.

Micro computer tomography

Mussel plaques were fixed in 70% ethanol and stained with 1% iodine in 96% ethanol modifying the staining protocol included in Metscher (17). Specimens were scanned at a voltage of 50 kV and a current of 198 μA without filter using a SkyScan 1172 micro-CT (Bruker, Kontich, Belgium). Scanning was performed in 96% ethanol as a scanning medium. Images were acquired at a pixel size of 2.55 μm with a camera binning of 1×1. The exposure time was 316 ms, and scans were performed for a full rotation of 360°, a frame averaging of 5 and a rotation step 0.24°. Projection images were reconstructed into cross-section images in a range of attenuation coefficients of 0–0.258318, with a beam-hardening correction of 59%, smoothing of 2, and ring artifact correction of 20.

Image and data analysis

TEM raw image files got size readjusted and converted to 8-bit files reducing the file size from 41 MB to 2.6 MB using FIJI (v2.3.0/1.53f51;). The images where then stitched together using the pairwise stitching plugin in FIJI. The final stitching was made using Adobe Illustrator CC 2015 (v19.0.0), creating a large panel consisted of 17 images. Manually editing and thresholding the image created a new duplicate image consisting only the background. The background was then subtracted from the original panel using the image calculator tool in FIJI. The large panel was split into 3 images (sections) in order to make processing more efficient. Each section was processed using ilastik (v1.4.0b27). Training the neural network algorithm to distinguish objects by annotating pixels, transformed the grayscale image to a binary one. Binary images were restitched together using Adobe illustrator into the binary panel. The

binary panel was analyzed using the analyze particle tool in FIJI. The results of the calculation were plotted into a Histogram using a custom script in Matlab (R2019b v9.7.01190202).

Optical microscopy image files were converted to 8-bit files and got stitched using the pairwise stitching plugin in FIJI. The background was manually subtracted using the image calculator tool in FIJI. Further processing involved the image segmentation (binary image) with ilastik and the analyze particle function in FIJI. Histograms and fits were done in Matlab.

III. Results

Micro computer tomography scans presented a 3D visualization of the fixed samples (Fig. 4). The resolution of the sample in volume pixels (voxels) presented no benefit to the analysis as the maximum output resolution is 1 μm^3/voxel. The pore diameter has been shown to be about 2 µm which would imply that a single pore would be non-distinguishable. This is proven by Fig. 4C were a cross section of the samples displays no signs of the porous interior of the plaque.

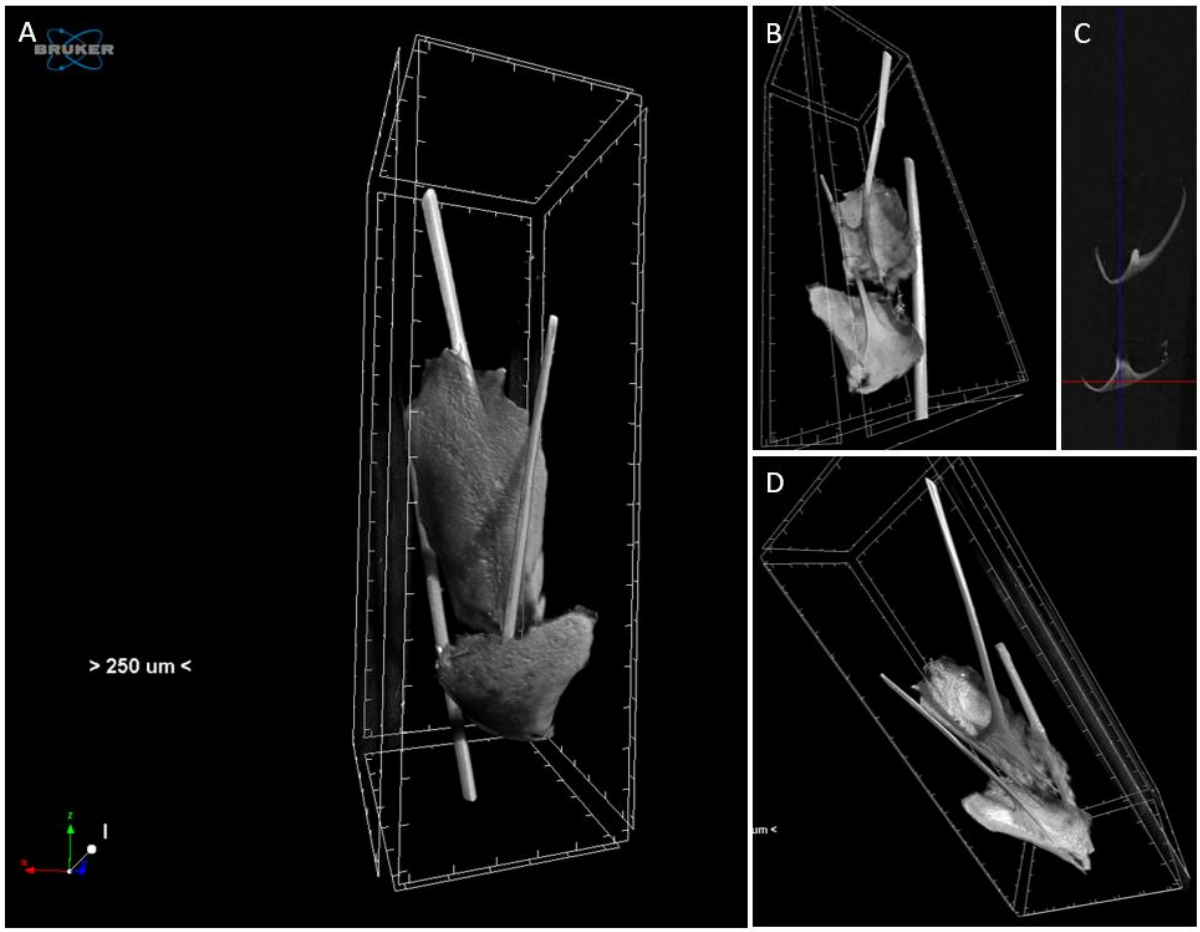

Fig. 4 Micro-CT scan 3D images of Byssal plaques (A), (B), (D) present the 3D analogue in different orientations at 250 µm. (C) Cross-section of the samples exhibiting the interior.

The obtain the desired resolution, I turned to electron and optical microscopy. Partially overlapping raw regions of interest were gathered from thin sections (1 µm and 100 nm thick). These were later stitched together for analysis. Image stitching allowed for the composition of high-definition sections.

Hence, a large area of the sample can be displayed at once exhibiting in great resolution the pores and the surrounding protein (Fig.5).

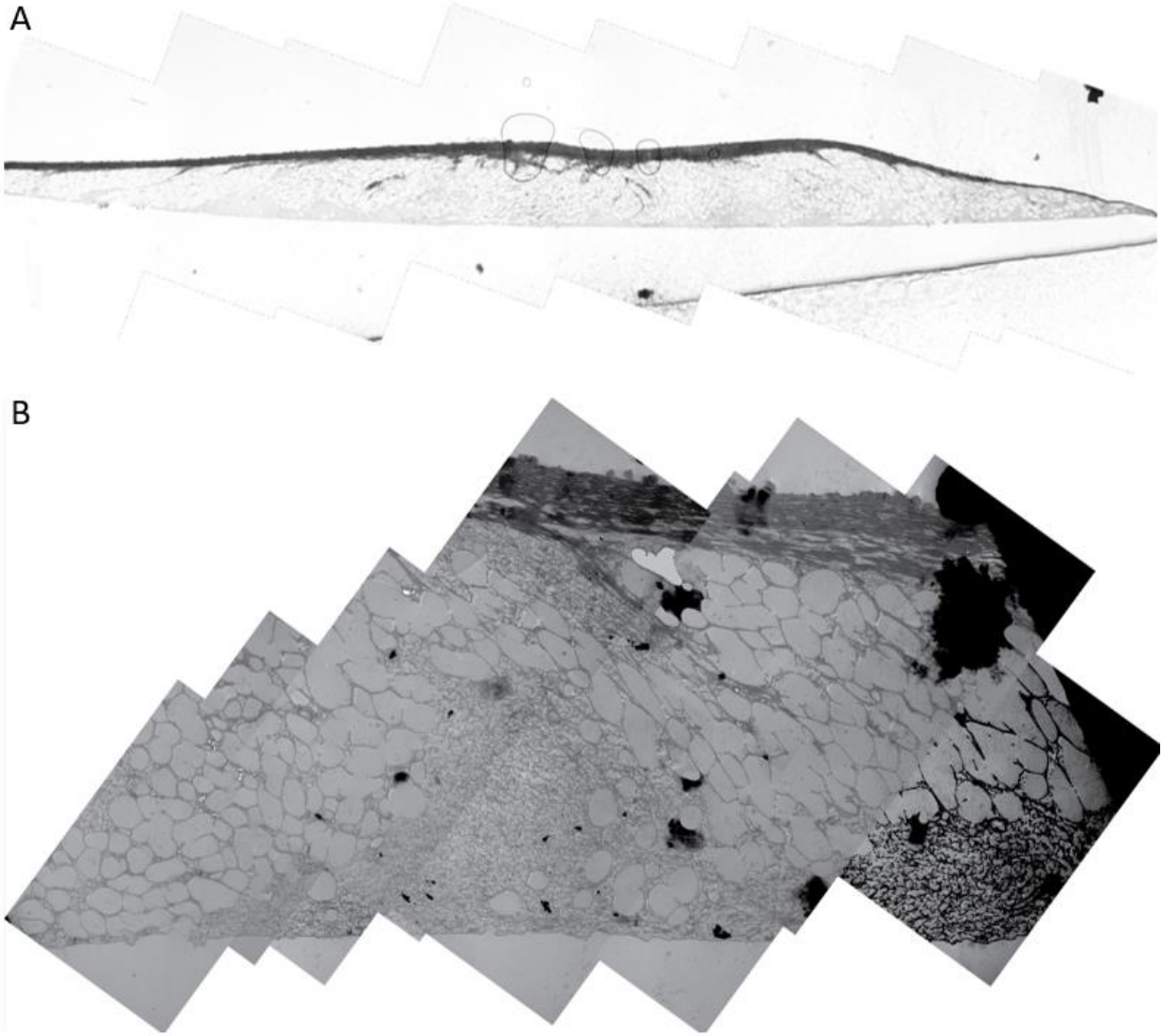

Fig. 5 Stitched raw images (A) Plaque section from optical microscope ($\sim 1\ \mu m$). thick. (B) TEM images stitched together exhibiting a large area of the plaque ($\sim 0.1\ \mu m\ thick$). Sections are consecutive slices from the same sample separated by few μm.

The stitched images (Fig. 5A, B) were post-processed by ilastik and FIJI into simple segmented images each with a different feature (Fig. 6). This allowed for a more accurate visual representation of the large vs the small mesh pore regions aiding with the analysis. In the optical microscopy panel (OMp) (Fig. 6A) there is sufficient contrast between large pores after processing (Fig. 6B, C). ~~whereas~~ A more detailed illustration of the same section is shown in the TEM panel (TEMp) (Fig. 6D-G) which allowed for an accurate and precise count of the area of both small and large pores. The area fraction, the number of pores and the surrounding walls (with the cuticle) per sample were calculated by using the corresponding segmented images (Fig. 6B, C, E, G).

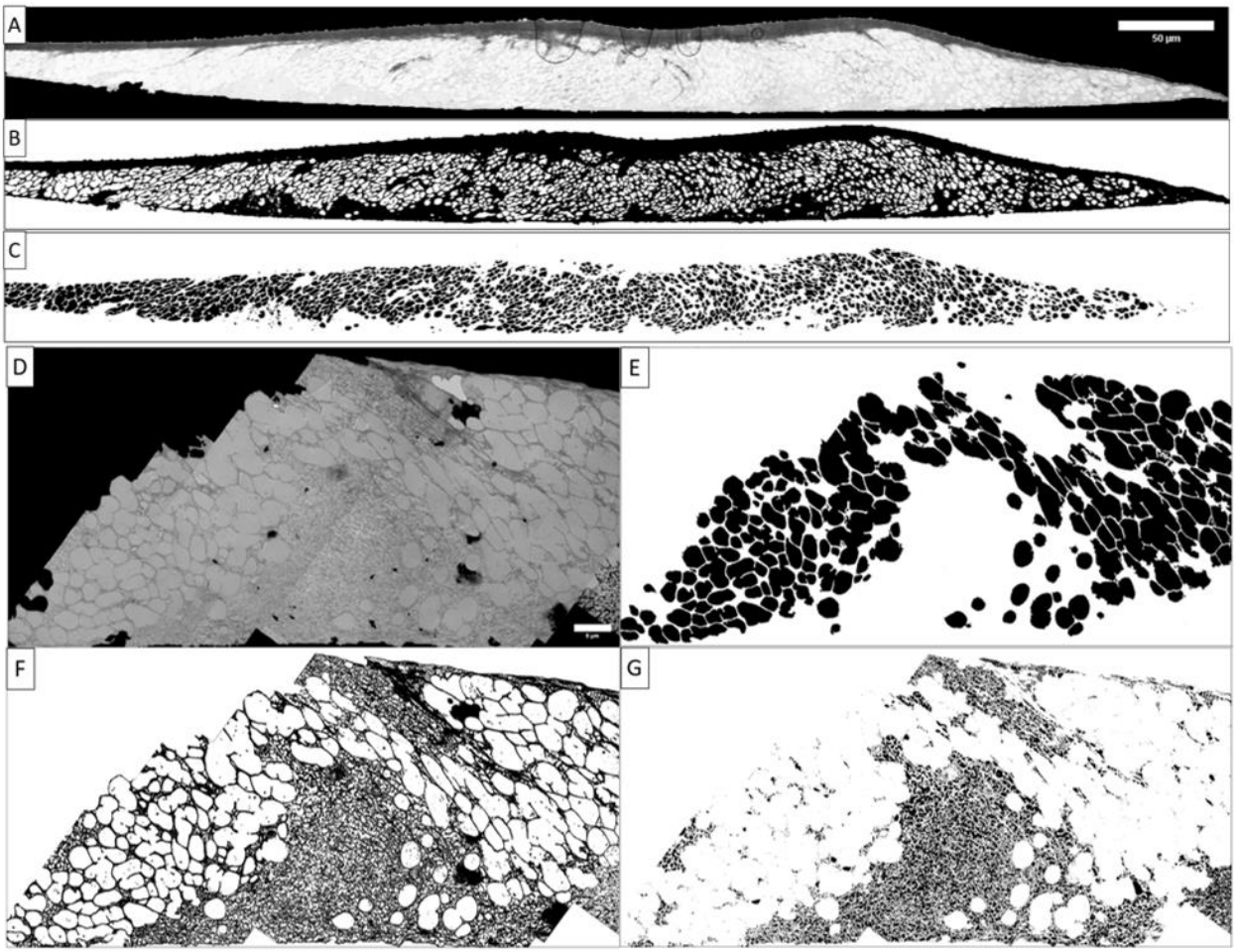

Fig. 6 Segmented images (A) Stitched optical microscope image in black background with 50 µm scalebar. (B) Simple segmented image showing the protein network. (C) Segmented image displaying only pores. (D) Stitched TEM image excluding incomplete edge pores with a 5µm scalebar. (E) Segmented image displaying large pores. (F) simple segmented image showing the protein network. (G) Segmented image displaying only small pores.

Image analysis

Optical microscopy analysis

Using the analyze particle function in FIJI on the segmented optical image (Fig. 6C) the area values ($pixel^2$) of each pore were calculated. After removing some noise or really small pores of dense network by excluding values below 77 $pixel^2$, the thresholded data were converted to μm^2 and plotted into a histogram on a linear and a logarithmic x-scale. The plotted data were fitted by 3 curves. A gaussian a stable and a nonparametric curve. The nonparametic fit is a smooth curve through the data calculated by Curve Fitting Toolbox ™ in Matlab (18). The stable fit is an application of the Generalized Central Limit Theorem and this type of fitting is suitable for skewed distributions (19). Percentages of the total sample present in the image and the features present per sample volume were calculated using Matlab.

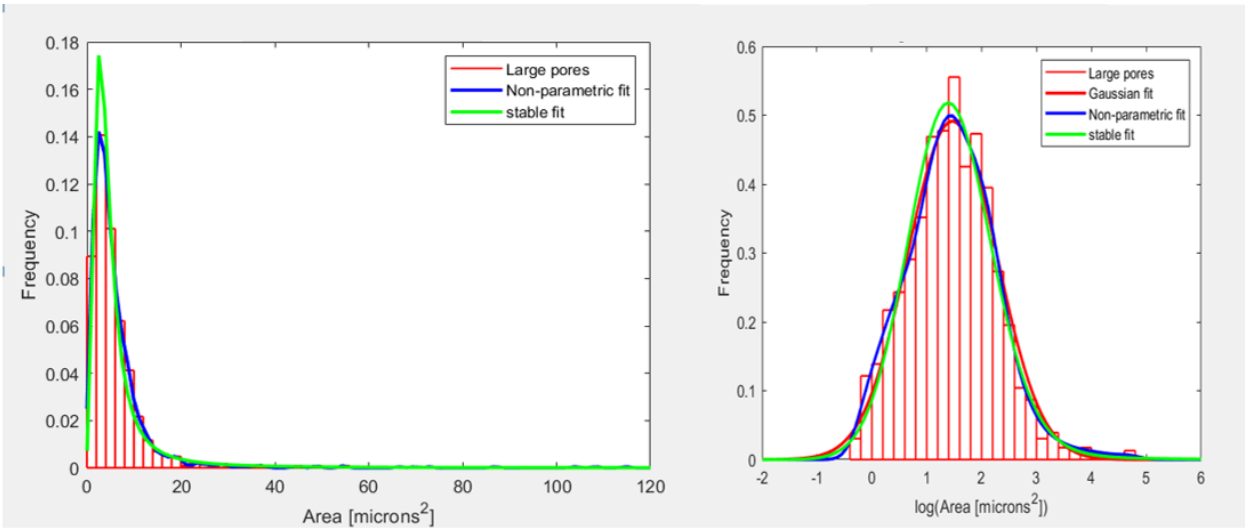

Fig. 7 Area distribution functions of optical microscopy panel. (Left) Linear scale histogram. (Right) Semi-logarithmic scale histogram showing the log-normal fit to the distribution of large pore areas.

Table. 1 Quantification analysis of optical microscopy panel (OMp).

Background [%]	Sample, including cuticle [%]	Large Pores per sample [%]	Small Pores per sample [%]	Protein per sample [%]
38.5	61.5	33.3	0.4	66.3

TEM panel analysis

Images 6E and 6G were analyzed with the "analyze particle" function in FIJI which enables the area values ($pixel^2$) of each pore to be calculated. A threshold of 30 pixels^2 was applied in order to clear some noise. The resulting data were converted to μm^2 and plotted into a histogram. The wide distribution of values on a linear scale produced unclear results and therefore the data were plotted on a logarithmic scale fitted by two curves (Fig.7). Percentages of the total sample without the cuticle (Fig. 6D) were calculated, as well as the percentages of features present per sample volume. Results are summarized in Table 2.

Table. 2 Quantification analysis of transmission electron microscopy panel (TEMp).

Background [%]	Sample, excluding cuticle [%]	Large Pores per sample [%]	Small Pores per sample [%]	Protein per sample [%]
26.7	73.3	55.7	18.6	25.7

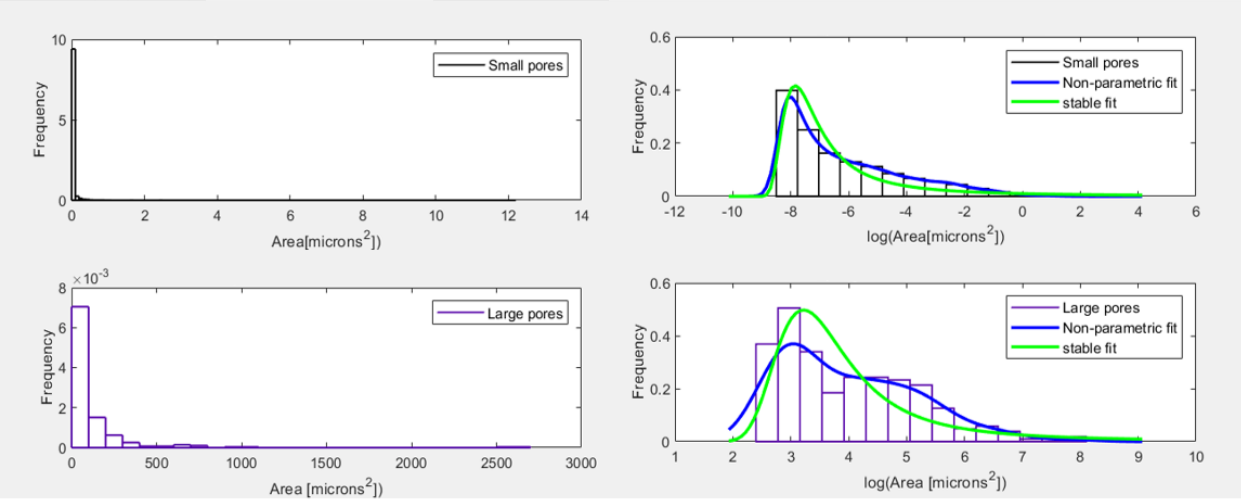

Fig. 8 Area distribution histograms of TEM panel. (Left) Linear scale histograms of the small and the large pores. (Right) Semi-log plots of the doubly porus plaque with 2 curves fitted.

Pore quantification and architecture

From the data gathered from each panel we can calculate each feature based on the accuracy each method provides. Therefore, a more accurate measurement of the number of large pores would emerge from the optical microscopy panel (OMp) due to the fact that it provides a larger ~~better~~ better in what respect? avoid using words like "different" or "better" and prefer more accurate alternatives field of view when quantifying the number of ~~for~~ large pores. In contrast, quantification of the small pore sections of the plaque can be calculated by the transmission electron microscopy panel (TEMp). Measurements are summarized at the table below (Table 3).

Table. 3 Pore count and area quantification of data images

Image Fig.5	Total Number of Pores counted	Large Pores [%]	Small Pores [%]	Protein [%]
B - OMp	1145	33.3	0.5	66.2
F - TEMp	12787	55.7	18.6	25.7

Reviewing the data of table 3, it is obvious that the ability to distinguish both kind of pores of the TEM imaging is superior, counting 12787 pores in an $(81.8 \times 40.1)\mu m^2$ ROI as opposed to 1145 in an $(634.0 \times 56.3)\mu m^2$ ROI using optical microscope image method. The small pore calculation with the OMp method proves to be an under estimate due to the low resolution of the small pore sections. Hence, the actual small pore data areas are included in the protein precent measurement making the protein percent measurement an overestimate.

I wished to directly compare the two methods using comparable areas. Focused solely on the comparison of the large pore probability distributions (which both methods seem to measure/detect) a section of the OMp image is cropped and used for the analysis (Fig. 7). Taking into consideration that only 73% of the TEMp image is represented by the sample (Table 2) the OMp is cropped accordingly (Fig. 9). To compare the two, an area distribution histogram is plotted (Fig. 9).

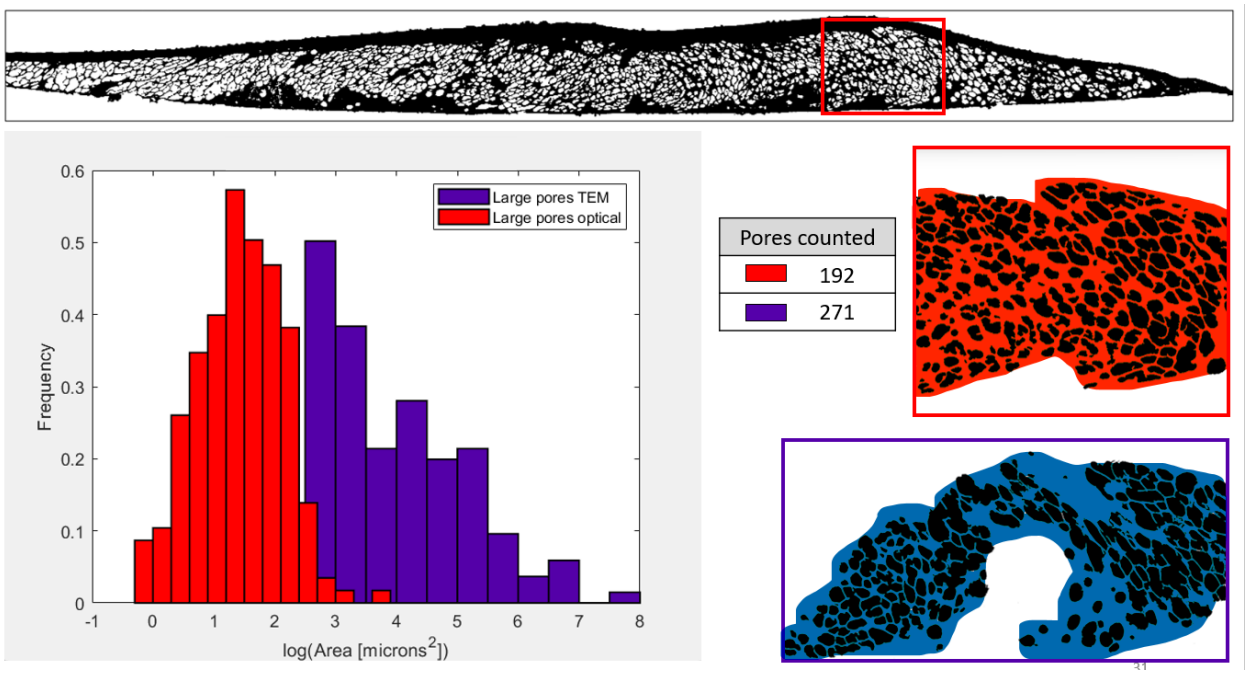

Fig. 9 Large pore density and architecture relation. (Top) Segmented section of the OMp cropped in order to possess roughly the same area for comparison. (Left) Logarithmic scale area distribution of the large pores present in the OMp and the TEMp respectively. (Mid) pores counted for the histograms plotted. (Right) Corresponding images.

Taking a closer look, it is obvious that the two histograms do not match despite the fact that they both represent area distributions of the large pores. The histogram from TEM (purple) appears to have a wider distribution indicating a broader value rage. Meaning that the pores in the TEMp (purple image) have a larger variety of sizes compared to the OMp (red image). In addition, the mismatch of the histograms indicates that TEMp presents overall larger pores, which can be confirmed by comparing the two images. The shape of the histograms gives information of the pore size density. A bell-shaped distribution of pore sizes exhibited in histogram on the left hints that the majority of pores have the average area value. On the contrary the right histogram, implies that the majority of pores resolve at the lower bound of area values with the rest gradually decreasing in count but increasing in size. Interestingly enough, even though the sections examined have about the same sample area, the pore density is different despite the fact that these two sections are almost identical in terms of where they are located in the plaque. This implies that for this sequential pair of sample sections, the pore density differs. However, this difference is due to the thickness of the sections of each method. The optical image creates a smaller projection of pores compared to the TEM image. Thus, the TEM image has the best resolution, but its histogram has limited data.

Estimating pore volume fraction from 2D images.

Determining an accurate estimation of the volume of each pore of the byssal plaque would require an exhaustive series of parallel sections throughout the whole sample. These sections should be then individually analyzed tracing each pore in order to reconstruct the 3D analogue form 2D images. However, this approach is almost impossible to be executed and the measurements would be sample specific. Hence, using stereology principles a representative estimation can be achieved giving an overall insight of the sample's structure. In order to create a uniformly random sampling window a series of parallel sections would be cut through the sample a fixed distance, T units, apart (9).

Here, 10 consecutive sections about 1 μm thick (T=1 μm) were obtained. Therefore, each face of the sections is spaced 1 μm apart from the previous. With the aid of optical microscopy, raw images of the sections were gathered and were later stitched together to create individual high quality image sections (Fig. 10). Postprocessing the images (Fig. 10) with ilastik and FIJI yielded binary images of the sections (Fig. 11) allowing for a clear definition of the pores.

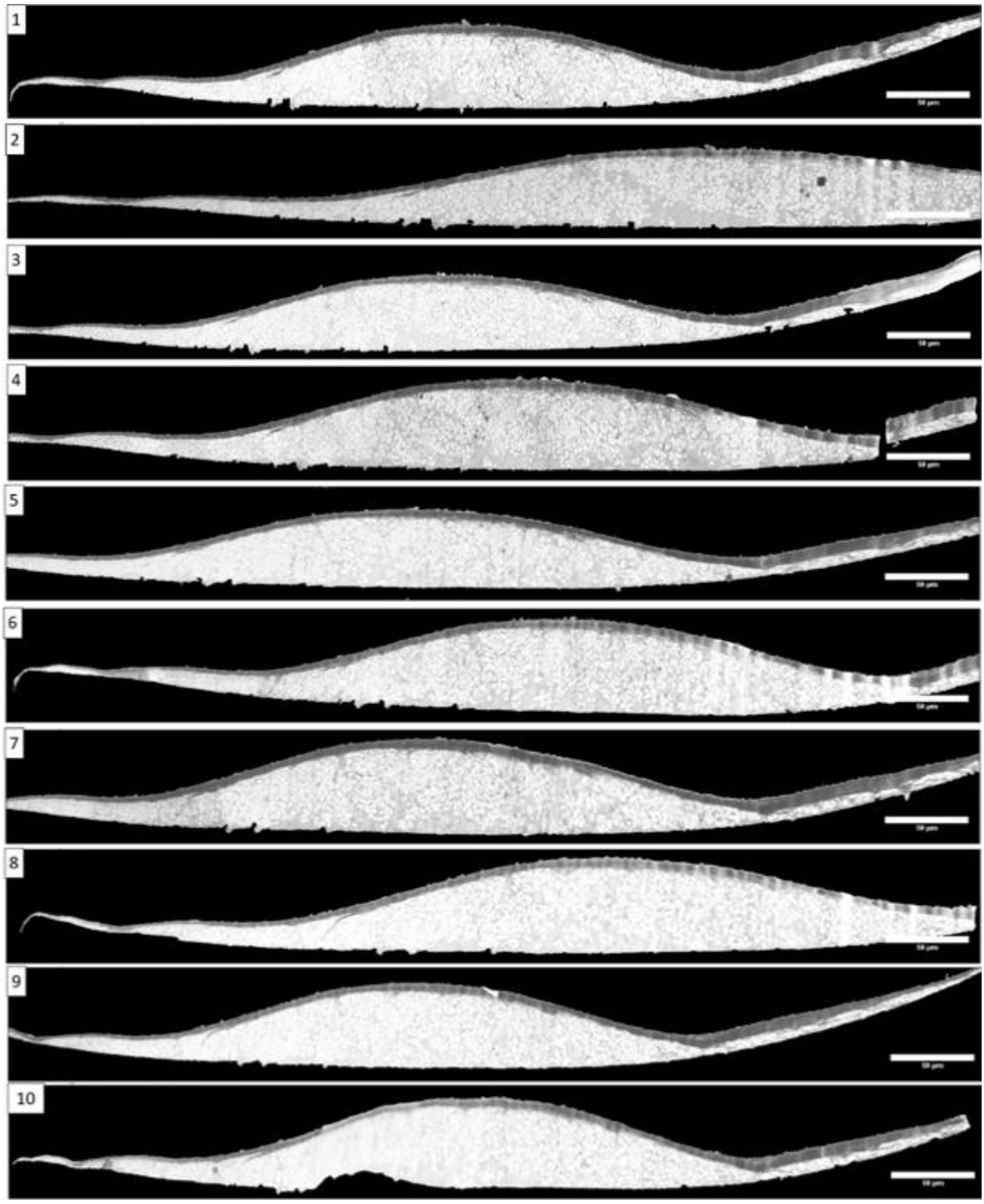

Fig. 10 Consecutive parallel sections 1 μm thick (1-10)

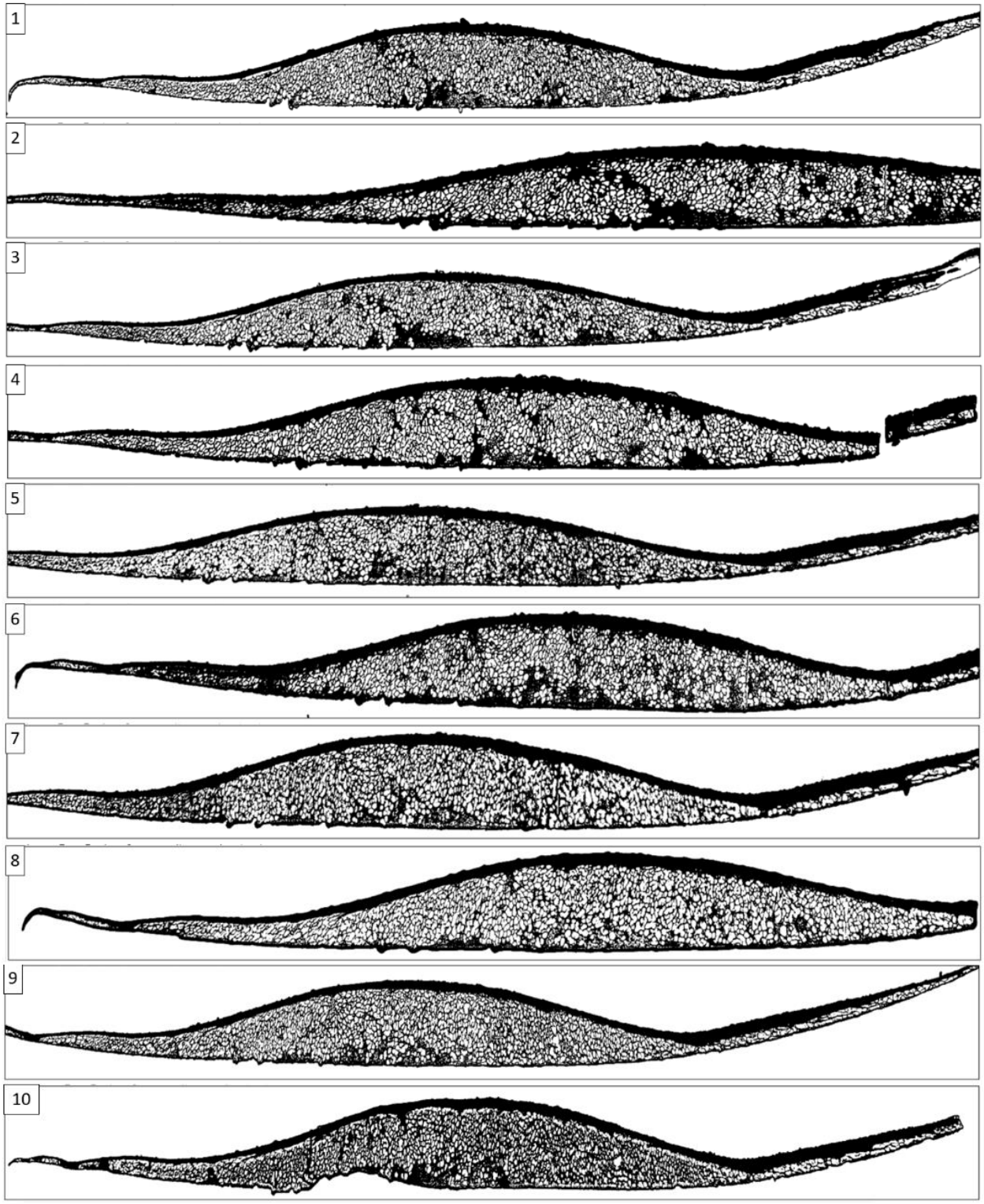

Fig. 11 Postprocessed sections binary images of consecutive sections (1-10)

The consecutive sections provide statistical information. Given that the pore diameter is comparable to the thickness of the sections, a visual, qualitative correlation could be determined by plotting the area distribution of pores of each binary section in a semi-log plot (Fig.11). The correlation parameter between sections at various distances highlights the similarities between pores at various sections while simultaneously providing insight of possible numeric pore density fluctuation patterns. The sets examined consisted of a sequential pair comparison of sections 1,2,4,5 (Fig.14), an isotropic sample selection (every 2) involving sections 1,3,5,7 (Fig.12) and two random sets (Fig. 13,15).

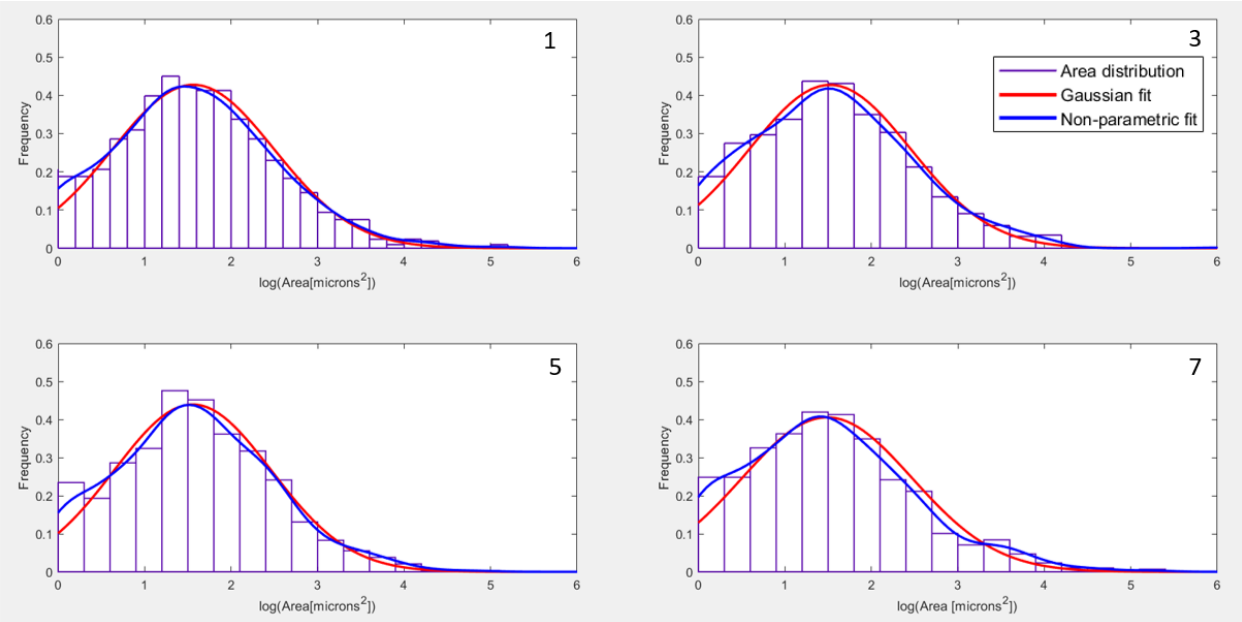

Fig. 12 Histograms with lognormal fits for the large pores featuring sections 1,3,5,7

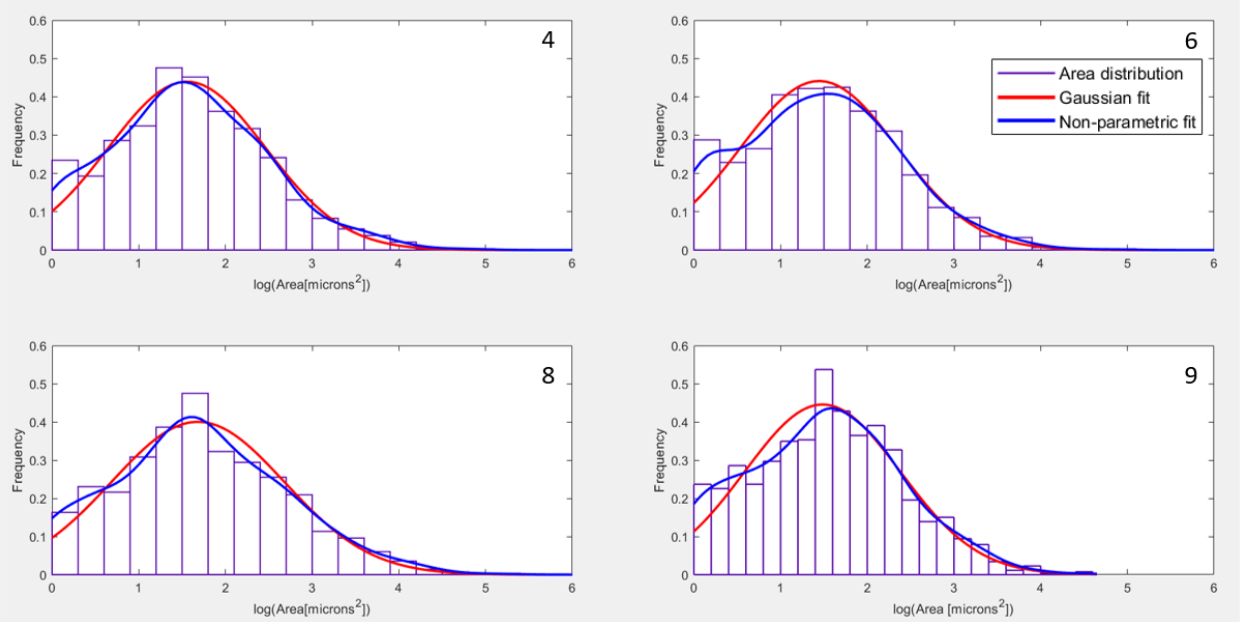

Fig. 13 Histograms with lognormal fits for the large pores of sections 4,6,8,9

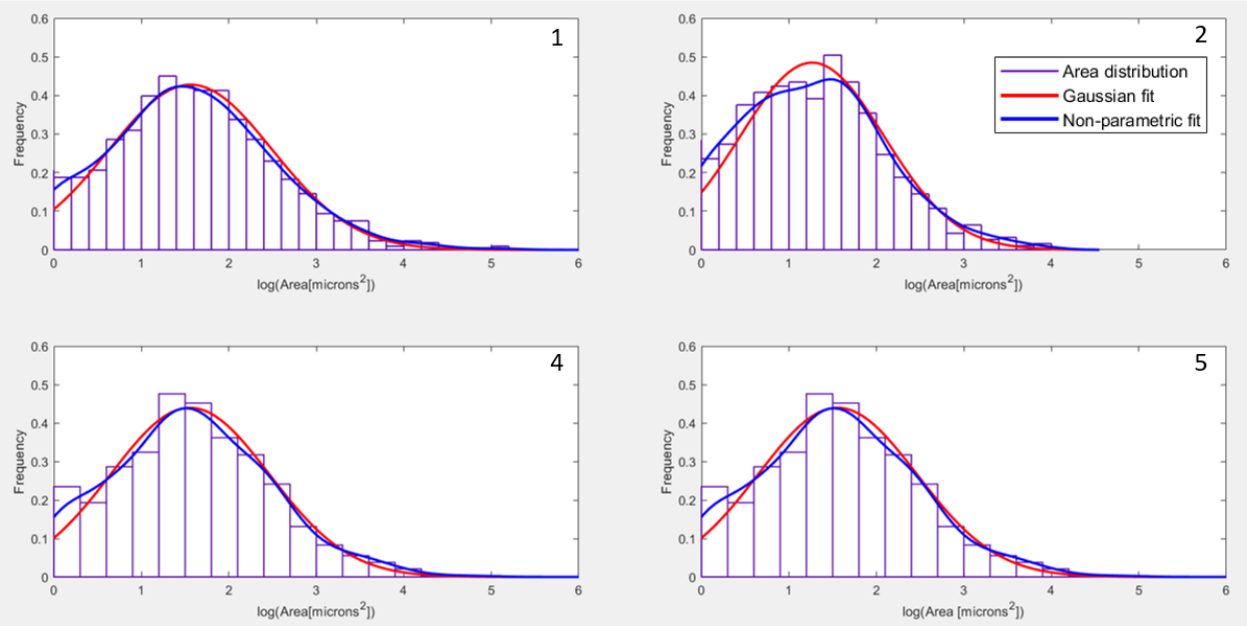

Fig. 14 Histograms with lognormal fits for the large pores of sections 1,2,4,5

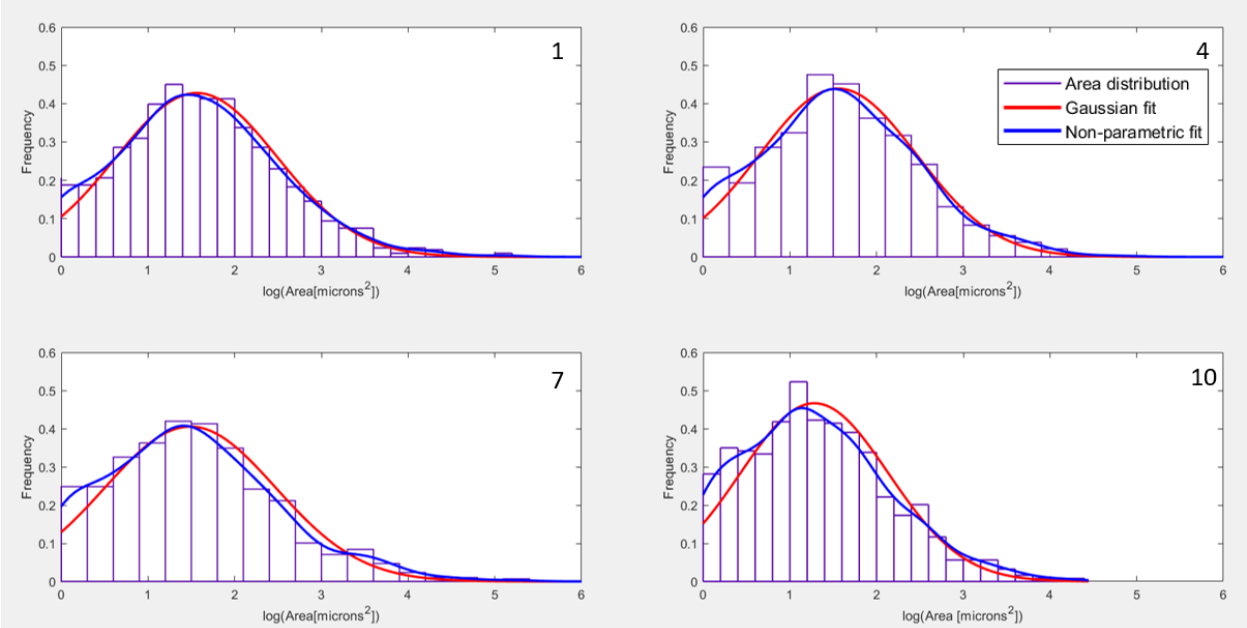

Fig. 15 Histograms with lognormal fits for the large pores of sections 1,4,7,10

Close examination of the semi-log area distributions (Fig.12 -15) reveals a strong correlation between the sections since all histograms have the same width You have the Gaussian fits, so you can state the mean μ, the standard deviation σ, the height A for all of them in a table with a peak frequency ranging between 0.4-0.5.

Moreover, we can estimate the total volume fraction of the pores by calculating the total area covered by the pores and diving by the sample area of each section. The volume of pores per sample for a given section would be given by the following equation [1].

$$V_v(pore, sample) = \frac{volume\ of\ phase\ of\ pores\ in\ the\ sample}{volume\ of\ sample} \quad [1]$$

However, the volume of pores is derived by the area of each pore multiplied by the thickness of each section. Hence,

$$[1] \Rightarrow V_v(pore, sample) = \frac{T \cdot A_p}{T \cdot A_s} = \frac{A_p}{A_s}$$

Were,

- T: is the thickness of the section [μm]
- A_p: Total area of the large pores inside the sample [μm^2]
- A_s: The area of the sample section

The measurements are summarized at the table below.

Table. 4 Total area measurements of the large pores and the sample area (with the cuticle) of each section.

Section	Total area of large pores [10^3 μm^2]	Sample area [10^3 μm^2]
1	8.3042	57.637
2	4.7760	38.580
3	8.0735	60.369
4	7.1646	43.150
5	7.1646	53.093
6	6.6811	44.115
7	7.8019	46.141
8	8.5991	40.389
9	8.8584	60.651
10	6.7789	59.409
Mean	7.4202	50.351

Using the data from Table. 4 the estimated total pore volume fraction is:

$$\hat{V}(pores, Sample) = \frac{\sum_{i=1}^{10} A_T(pore, i)}{\sum_{i=1}^{10} A_T(sample, i)} = \frac{7.4202 \cdot 10^3}{5.0351 \cdot 10^4} \cong 0.15$$

This estimation is not unbiased since all the pore areas were collected by the binary images of the sections created in ilastik. The trainable segmentation algorithm output was heavily influenced by human

interaction and bias though the training process. By collecting all the data directly to the analysis and by applying a threshold the bias was curried over.

Pore Shape

Two-dimensional (2D) sections help us characterize the spatial structure and size of the particles inside the plaque. However, it has been a common practice to apply stereological 2D to 3D conversion methods derived from spherical polydisperse systems where the particles of the system have the same shape but differ in size (Fig. 16).

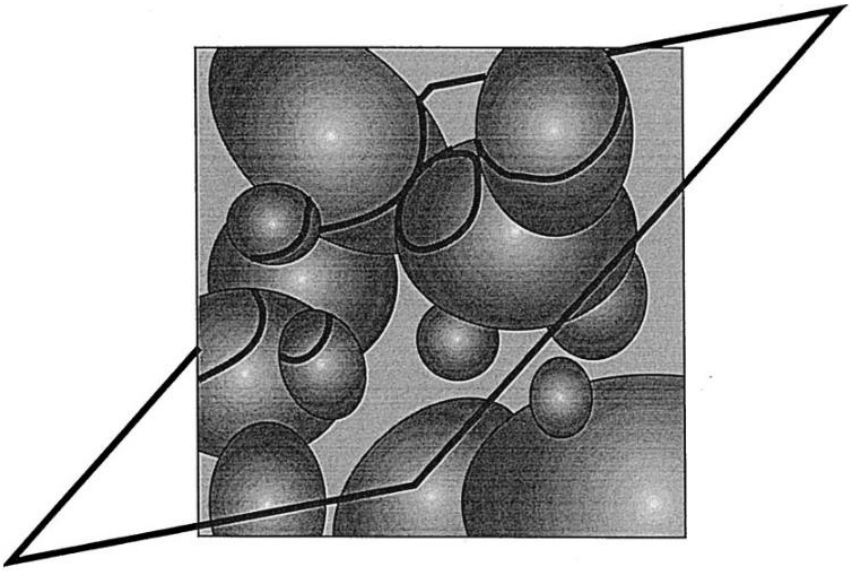

Fig. 16 Random plane dissecting a distribution of particles. The particles are not intersected trough their center (18).

When a distribution of particles is randomly cut by a plane, the intersected areas of each particle are not the same. The cross-sections made can be divided into a probability distribution, according to their size. This distribution is normally described by a finite number of discrete size classes. A monodisperse system of particles (Fig. 17) would exhibit the maximum probability of intersections through the center of the particles. Consequently, in a probability distribution function, the largest cross-section size class would testify the actual 3D size of the sphere which would have the diameter of the largest circular cross-section. The probability distribution for a sphere of random cross-section sizes can be derived (Fig. 17).

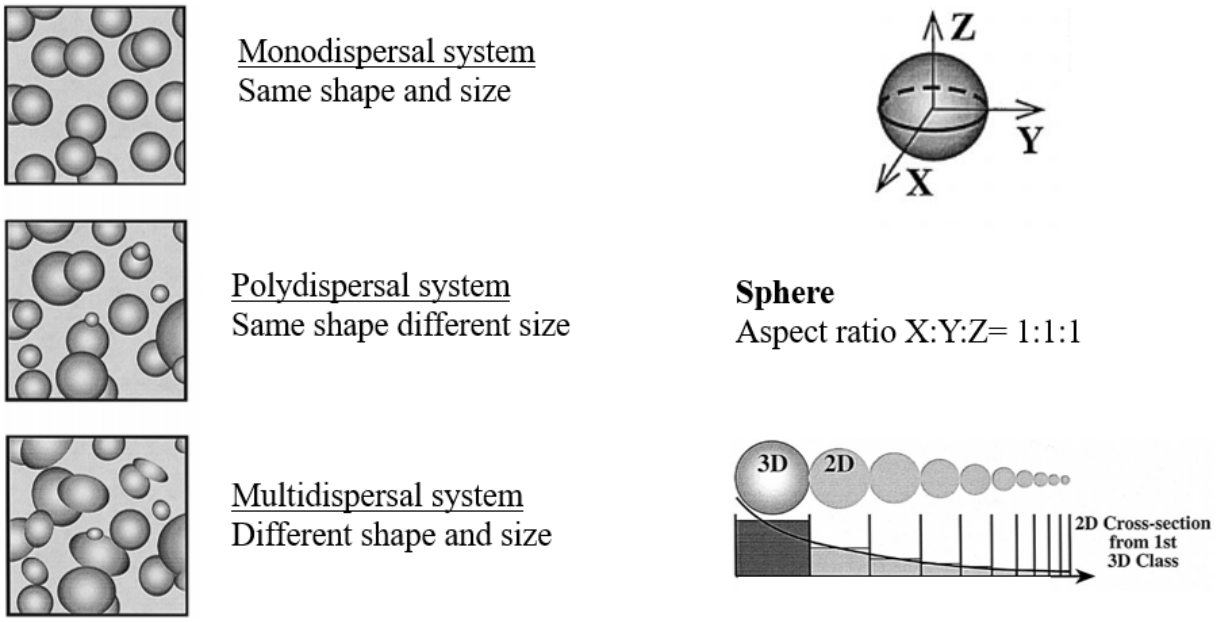

Fig. 17. 2D to 3D conversion (Left) various dispersion systems (16). (Right) probability distribution of a sphere (18).

Assuming that a polydisperse system is the sum of monodisperse systems, the probability distribution of the mean tangent diameter of the particles normalized by the diameter value of largest class of a unimodal sphere, can be plotted (Fig. 17). Expanding further a multidisperse system can be the sum of many polydisperse systems. Hence, we can estimate the shape of the pores in a plaque by comparing the probability distribution of the normalized mean tangent diameter values of the pores to literature (Fig.18).

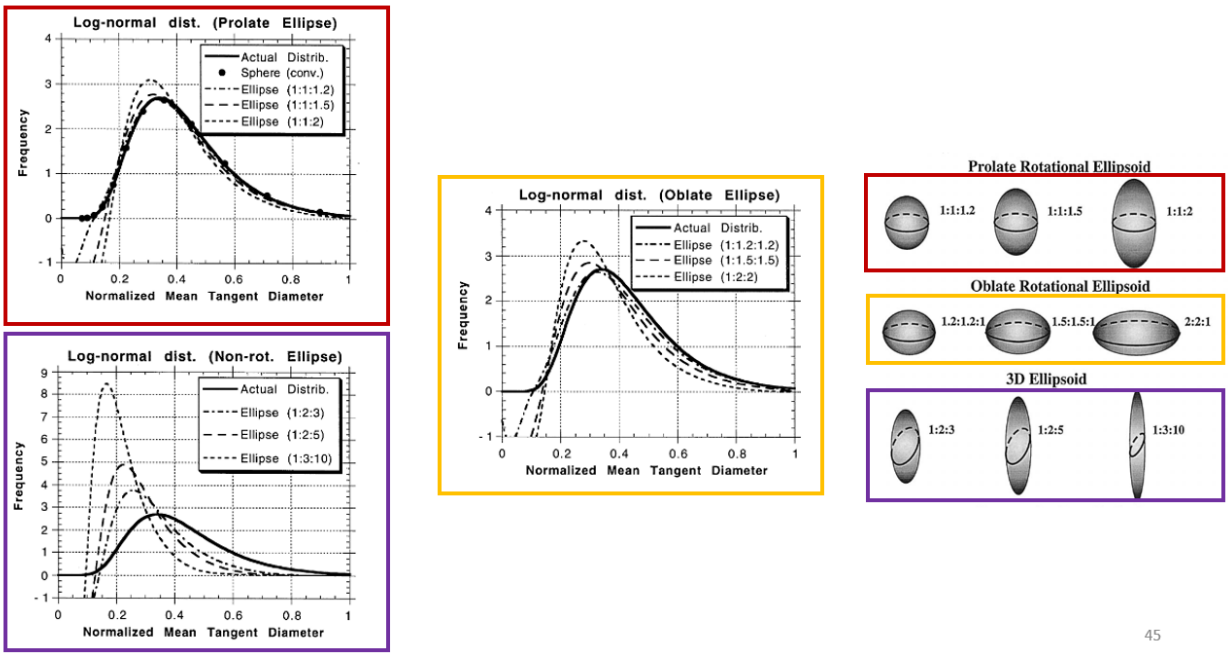

Fig. 18. Probability distribution functions of various shapes (16).

IV. Conclusion

The mussel byssal plaque is a remarkable material with adhesive properties derived from its double porous inner structure. Stereology techniques combined with electron and optical microscopy imaging of thin sections provide a tangible source of information regarding the architecture of the plaque. Although a powerful tool the accuracy of the estimation lays on the section sample selection and its uniformly random distribution of pores in order to achieve an estimate with minimal bias. Other methods of estimating pore distribution and size are scanning techniques such as mercury porosimetry and micro computer tomography however not without their limitations. Statistical analysis on 2D sections can easily converted to 3D volume fraction estimations taking into account the sections thickness.

In the future, more stereology methods can be applied such as the Cavalieri estimator of volume which would provide an unbiased estimation of the plaques pore volume fraction. Also, the probability distributions of the mean diameter of the pores will be plotted to give an estimate of the shape of the pores compared to the distribution functions of spherical and ellipsoidal particles. The results of all the estimations will be compared with nano computer tomography (nano CT) and focused ion beam scanning electron microscopy (FIB-SEM) in hopes of constructing an actual 3D printed model of the byssal plaque or a digital 3D analogue for strength stain simulations.

V. Bibliography

1. J. H. Waite, Mussel adhesion - Essential footwork. *Journal of Experimental Biology* **220**, 517–530 (2017).
2. Timothy J Deming-"Mussel byssus and biomolecular materials Deming 101." *Current Opinion in Chemical Biology*, 3:100-105 (1999).
3. E. Filippidi, *et al.*, The microscopic network structure of mussel (Mytilus) adhesive plaques. *Journal of the Royal Society Interface* **12** (2015).
4. N. R. Martinez Rodriguez, S. Das, Y. Kaufman, J. N. Israelachvili, J. Herbert Waite, Interfacial pH during mussel adhesive plaque formation. *Biofouling* **31**, 221–227 (2015).
5. T. Priemel, *et al.*, "Microfluidic-like fabrication of metal ion-cured bioadhesives by mussels."
6. A. Ghareeb, A. Elbanna, On the Role of the Plaque Porous Structure in Mussel Adhesion: Implications for Adhesion Control Using Bulk Patterning. *Journal of Applied Mechanics, Transactions ASME* **85** (2018).
7. J. H. Bernstein, E. Filippidi, J. Herbert, W. Cd, M. T. Valentine, Effects of sea water pH on marine mussel plaque maturation. *Royal Society of Chemistry* (*Soft Matter)* **16**, 9339 (2020).
8. "Poroelastodynamics" in *Theory and Applications of Transport in Porous Media*, (Springer International Publishing, 2016), pp. 475–571.
9. V. Howard, M. Reed, Estimation of reference volume using the Cavalieri method. *Unbiased Stereology*, 53–70 (2021).
10. H. Giesche, Mercury porosimetry: A general (practical) overview in *Particle and Particle Systems Characterization*, (2006), pp. 9–19.
11. What is Micro-CT? An Introduction | Micro Photonics (June 2, 2022). https://www.microphotonics.com/what-is-micro-ct-an-introduction/
12. cellpose (May 31, 2022). https://www.cellpose.org/
13. CountEm | Efficient and Unbiased Estimation (May 31, 2022). https://countem.unican.es/
14. Trainable Weka Segmentation (May 31, 2022). https://imagej.net/plugins/tws/
15. ilastik - ilastik (May 31, 2022). https://www.ilastik.org/
16. D. L. Sahagian, A. A. Proussevitch, 3D particle size distributions from 2D observations: Stereology for natural applications. *Journal of Volcanology and Geothermal Research* **84**, 173–196 (1998).
17. B. D. Metscher, Micro CT for comparative morphology: Simple staining methods allow high-contrast 3D imaging of diverse non-mineralized animal tissues. *BMC Physiology* **9**, 1–14 (2009).
18. Nonparametric Fitting - MATLAB & Simulink (July 13, 2022). https://www.mathworks.com/help/curvefit/nonparametric-fitting.html
19. Stable Distribution - MATLAB & Simulink (July 13, 2022). https://www.mathworks.com/help/stats/stable-distribution.html